

Article

Rapid Mapping of Rainfall-Induced Landslide Using Multi-Temporal Satellite Data

Mohammad Adil Aman, Hone-Jay Chu *, Sumriti Ranjan Patra  and Vaibhav Kumar 

Department of Geomatics, National Cheng Kung University, Tainan 701, Taiwan;
p68097103@gs.ncku.edu.tw (M.A.A.); p68107047@gs.ncku.edu.tw (S.R.P.); p68097064@gs.ncku.edu.tw (V.K.)

* Correspondence: honejaychu@geomatics.ncku.edu.tw

Abstract: In subtropical regions, typhoons and tropical storms can generate massive rainstorms resulting in thousands of landslides, often termed as Multiple-Occurrence of Regional Landslide Events (MORLE). Understanding the hazards, their location, and their triggering mechanism can help to mitigate exposure and potential impacts. Extreme rainfall events and earthquakes frequently trigger destructive landslides that cause extensive economic loss, numerous fatalities, and significant damage to natural resources. However, inventories of rainfall-induced landslides suggest that they occur frequently under climate change. This study proposed a semi-automated time series algorithm that integrates Sentinel-2 and Integrated Multi-satellite Retrievals for Global Precipitation Measurements (GPM-IMERG) data to detect rainfall-induced landslides. Pixel-wise NDVI time series data are analyzed to detect change points, which are typically associated with vegetation loss due to landslides. These NDVI abrupt changes are further correlated with the extreme rainfall events in the GPM-IMERG dataset, within a defined time window, to detect RIL. The algorithm is tested and evaluated eight previously published landslide inventories, including both those manually mapped and those derived from high-resolution satellite data. The landslide detection yielded an overall F1-score of 0.82 and a mean producer accuracy of 87%, demonstrating a substantial improvement when utilizing moderate-resolution satellite data. This study highlights the combination of using optical images and rainfall time series data to detect landslides in remote areas that are often inaccessible to field monitoring.



Academic Editor: Domenico Calcaterra

Received: 4 March 2025

Revised: 2 April 2025

Accepted: 8 April 2025

Published: 15 April 2025

Citation: Aman, M.A.; Chu, H.-J.; Patra, S.R.; Kumar, V. Rapid Mapping of Rainfall-Induced Landslide Using Multi-Temporal Satellite Data. *Remote Sens.* **2025**, *17*, 1407. <https://doi.org/10.3390/rs17081407>

Copyright: © 2025 by the authors. Licensee MDPI, Basel, Switzerland. This article is an open access article distributed under the terms and conditions of the Creative Commons Attribution (CC BY) license (<https://creativecommons.org/licenses/by/4.0/>).

1. Introduction

Landslides refer to the movement of slope materials, either natural rocks, soils, or a combination of the two, moving downward and outward [1]. These pervasive natural geohazards occur under the influence of gravity, often triggered by rainfall, earthquakes, volcanic eruptions, and human influences on slopes [2,3]. The impact of MORLE is often destructive and subject to exposure, infrastructure, and population density [4–6]. The threat associated with landslides is exacerbated in regions with unstable geology, steep terrain, and extreme rainfall [7,8]. Landslides not only cause immediate destruction to landscapes but also pose serious risks to infrastructure, human life, and ecosystems [9,10]. The human cost due to landslides is substantial; there is an estimated 1000 deaths and more than 200 thousand people have been affected worldwide due to landslides in the last two decades [11]. However, some reports indicate that this is an underestimation, with actual casualties reaching up to 56,000 between only 2004 and 2016 [9]. Based on the

statistics from the Unified Global Landslide Database (UGLD), from 1903 to 2020, a total of 37,946 recorded landslides resulted in 185,753 fatalities worldwide, with Asia and the Americas experiencing the highest number of events and casualties [12].

Numerous approaches for landslide monitoring, including Earth observation techniques, have been developed to aid in the estimation of landslide hazard and risk assessment to protect human life and natural resources [13–15]. For effective planning and the mitigation of the associated risks, landslide monitoring agencies can benefit from thorough information and spatio-temporal distribution from landslide inventories [16,17]. This distinction in triggering mechanisms (earthquake vs. rainfall) highlights the importance of using a tailored landslide inventory to address the distinct requirements of each event and analysis; however, rainfall-induced landslides (RILs) become more likely as a result of climate change compared to earthquake-induced landslides. The locations of landslides caused by rainfall may coincide with landslides caused by earthquakes on a particular hill-slope. The high peak ground acceleration during earthquakes tends to increase landslides near the top of the hills and ridges, while extreme rainfall that enriches water saturation near the base of slopes tends to stimulate landslides lower down the ridges [18,19]. Additionally, the high cost of obtaining high-resolution satellite data to precisely map the RIL is a contributing factor to the limited availability of RIL inventories [17]. Therefore, it is crucial to expand the analysis to include RIL inventories to allow for a more comprehensive comparison and to provide valuable data for RIL hazard assessment and mitigation.

Traditionally, field surveys, topographic analyses, and physical models have been used to detect and map landslides [6,14,20]. Manually mapping landslides is typically an accurate, useful, and systematically documented data source [14]; however, it is associated with time-consuming and labor-intensive surveys in inaccessible and hazardous terrain. The availability of digital landslide inventories is rather limited and is often based on news articles and social media [9,21], which might compromise the accuracy of marked locations. Furthermore, such landslides that happen outside of areas inhabited by people or in inaccessible terrains seldom have fatalities and often go unrecorded [22]. Optical remote sensing has been recognized as an efficient tool for landslide monitoring and detection in numerous studies [16,23,24]. Although clouds and shadows are a perpetual challenge for optical images, the growing amount of publicly available data, such as the Landsat mission and Sentinel-2, providing moderate-to-high spatial resolution, frequent temporality, and vast historical archives are compatible with comprehensive analyses [25,26].

In this study, remote sensing Earth observation data were used to detect RILs across ten cases worldwide, primarily in subtropical regions. We introduced a multi-temporal approach for RIL detection to generate RIL inventories when compared to those generated by high-resolution data. The approach is based on using satellite time series data to detect landslides rather than a traditional assessment of pre- and post-event images. The loss of vegetation due to RILs on hillsides is evident by a sudden drop in the NDVI time series data. This abrupt change, when correlated with extreme rainfall events, is leveraged to detect RILs. To account for the quality assessment of the detection, the algorithm is applied to eight cases with pre-existing inventories, and two new inventories are prepared in this study. This facilitates an explicit assessment of the inventories when compared with several manual or high-resolution inventories.

2. Materials and Methods

2.1. Study Area

Figure 1 shows ten distinct case studies from diverse global locations, predominantly within subtropical zones. Landslide events were triggered by heavy rainfall and typhoons. Table 1 shows a summary of the landslide inventories used in this study. The selected

cases met the requirements for the availability of sufficient satellite imagery before and after the event of intense rainfall or tropical cyclones, as clouds often obscure the clear sky during such events. The hillslope and rainfall information are shown in Table 2. Given that precipitation variability significantly influences landslide occurrence and vegetation recovery, we included sites with different rainfall patterns, ranging from high-intensity storms to prolonged monsoonal precipitation. Additionally, we aimed to select study sites from all regions in the subtropics, ensuring broad spatial representation and applicability. Rainfall statistics are derived from the GPM-IMERG data. Additionally, these cases also have well-documented landslide inventories in contemplation for development as well as a validation of the algorithm. The inventories were mainly compiled using drone-based surveys, aerial photography, and high-resolution satellite data such as Planet and RapidEye in certain studies (Table 1).

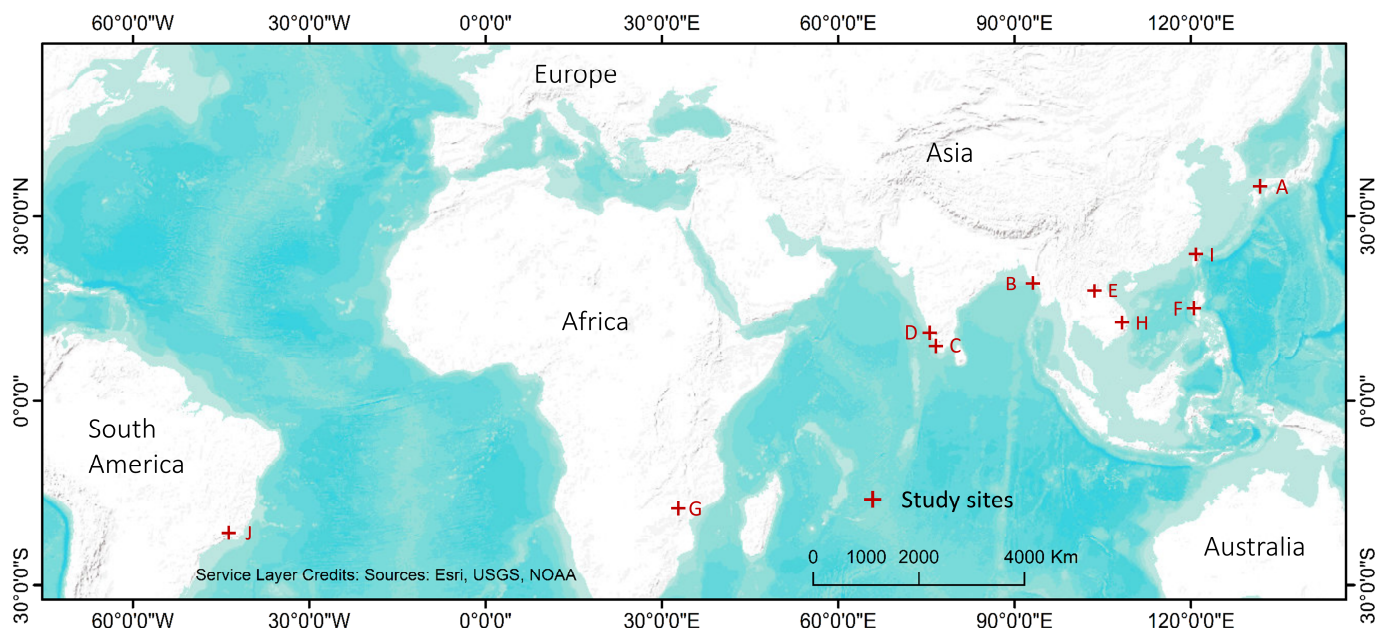


Figure 1. Study area map showing the distribution of locations considered for analysis.

Table 1. Summary of the landslide inventories used in this study in alphabetical order as marked in Figure 1.

	Location	Event	Date of Event	Reference Inventory	Source (Spatial Resolution)	Inventory Type	Total Mapped Area (km ²)
A	Hiroshima, Japan	Intense rain	28 June–9 July 2018	The Association of Japanese Geographers (2019) [16]	Drone/aerial imagery (varying)	Polygon	1940.3
B	Paung, Myanmar	Intense rain	28–30 July 2018	Amatya et al., 2022 [27]	RapidEye (5 m), Planet (3 m)	Points	84.3
C	Thrissur, India	Intense rain	7–18 August 2018	Emberson et al., 2022 [16]	Planet (3 m)	Polygon	1150.6
D	Kodagu, India	Intense rain	10–17 August 2018	This study	Sentinel-2 (10 m)	Polygon	187.3
E	Phonxay, Laos	Intense rain	28–30 August 2018	Amatya et al., 2022 [27]	RapidEye (5 m), Planet (3 m)	Points	317.8
F	Itogon, Philippines	Typhoon Mangkhut	15–20 September 2018	Emberson et al., 2022 [16]	Planet (3 m)	Polygon	382.6
G	Mutare, Zimbabwe	Cyclone Idai	15–19 March 2019	Emberson et al., 2022 [16]	Planet (3 m)	Polygon	923.7
H	Huong Viet, Vietnam	Intense rain	14–18 October 2020	Amatya et al., 2022 [27]	RapidEye (5 m), Planet (3 m)	Points	724.8
I	Yilan, Taiwan	Intense rain	15–17 October 2022	Taiwan Government Inventory	Multiple (6 m, 10 m, 30 m)	Polygon	26.8
J	Sao Paulo, Brazil	Intense rain	18–22 February 2023	This study	Sentinel-2 (10 m)	Polygon	49.7

Table 2. Rainfall and slope statistics for the cases discussed in the study. Rainfall statistics are derived from the GPM-IMERG data.

Location	Total Rainfall (mm)	Maximum Hourly Rainfall (mm)	Mean Rainfall Intensity (mm/Day)	Mean Slope (Degrees)	Maximum Slope (Degrees)
Hiroshima	879	25.71	73.25	19.4	53.9
Yilan	181	34.13	60.33	34.8	60.8
Itogon	762	45.15	127.00	33.4	57.5
Phonxay	549	11.6	183.00	32.2	62.8
Huong Viet	649	23.51	129.80	26.6	59.1
Paung	883	30.01	294.33	25.5	41.4
Thrissur	675	24.62	56.25	26.7	61.9
Mutare	418	29.11	83.60	25.8	57.4
Kodagu	742	15.83	92.75	16.1	45.5
Sao Paulo	251	13.62	50.20	26.3	51.2

2.2. Methodology

The proposed algorithm systematically detects rainfall-induced landslides (RILs) by integrating the Sentinel-2 NDVI time series with GPM-IMERG rainfall data. This approach ensures large-scale, consistent, and efficient mapping of landslides across diverse subtropical landscapes. The methodology consists of three main steps: (1) data acquisition and preprocessing, (2) landslide detection by integration of optical images with rainfall data, and (3) validation and accuracy assessment.

2.2.1. Data Acquisition and Preprocessing

The study utilizes freely available remote sensing datasets to ensure the broad applicability of the algorithm. The datasets employed are as follows:

A. Sentinel-2 optical imagery

Sentinel-2 Level-1C data were acquired and processed within the Google Earth Engine (GEE) due to its fine spatial resolution and quick revisit frequency covering multiple landslide-prone regions. Level-1C data were preferred over Level-2A due to their wider availability and global consistency. The images were preprocessed by applying atmospheric correction and cloud masking to ensure high-quality surface reflectance data. A critical challenge in using optical imagery is cloud contamination, which can obscure landslides. To address the cloud issue, we utilized a newly developed cloud masking algorithm, “All Clear with Cloud Score+” [28], to effectively eliminate cloud-contaminated pixels from the images. The algorithm enhances cloud detection and removal by utilizing probabilistic cloud scoring, allowing for better retention of valid surface observations compared to traditional threshold-based cloud masks. Its adaptive approach minimizes cloud contamination in optical imagery, making it ideal for time series analysis, vegetation monitoring, and land change detection in persistently cloudy regions. Figure 2 illustrates the effectiveness of the All Clear with Cloud Score+ algorithm in removing cloud contamination from Sentinel-2 imagery, with one case used from Northern and Southern tropical regions each, offering a significant improvement over the traditional cloud mask by eliminating thin clouds, haze, and cloud shadows, thereby enhancing the reliability of surface observations.

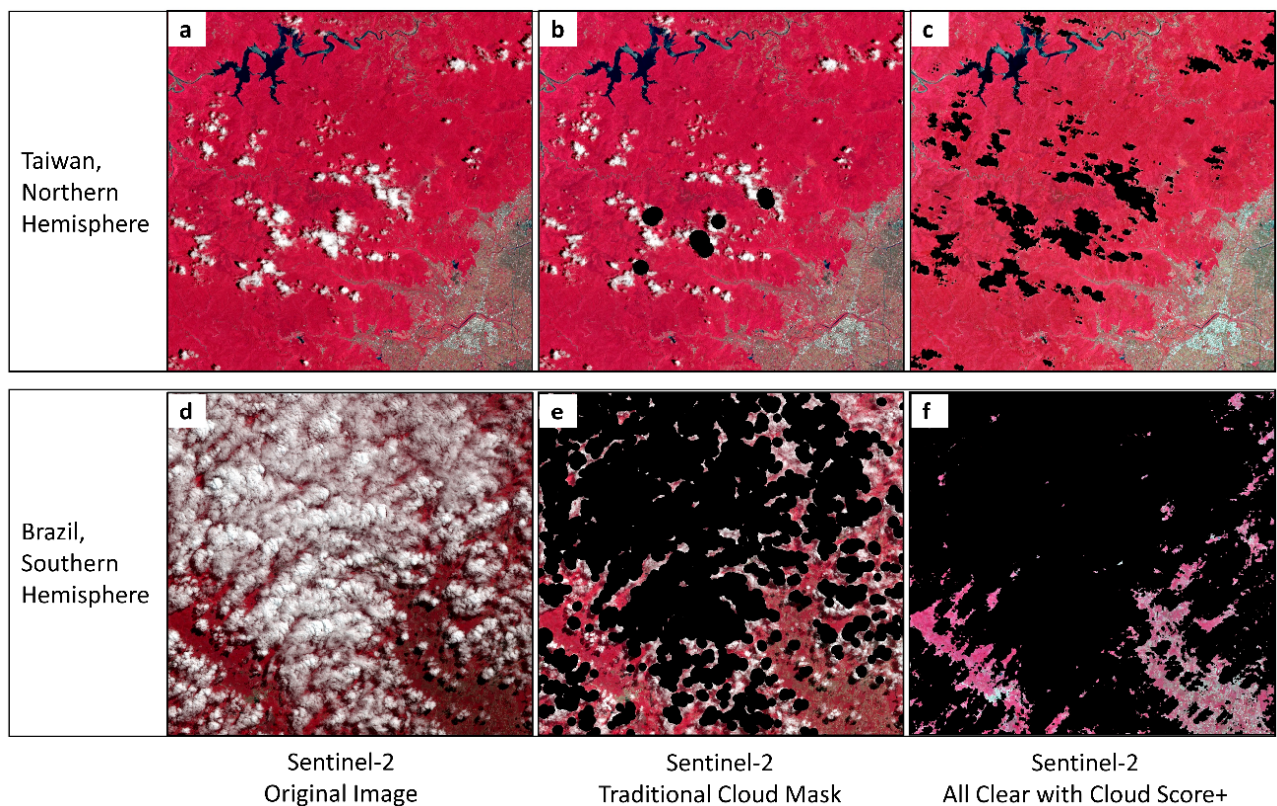


Figure 2. (a,d) are Sentinel-2 original False Color Composite (FCC) images, (b,e) are Sentinel-2 FCC images after cloud mask, and (c,f) are Sentinel-2 FCC images after “All Clear with Cloud Score+” mask.

In persistent cloud conditions, where images immediately after a landslide event were unavailable, monthly or bimonthly composite images were generated to provide an uninterrupted NDVI time series. This approach ensured a continuous temporal record, allowing for the accurate detection of abrupt vegetation changes associated with landslides. Notably, we were able to generate adequate clear imagery across all study sites without exceeding the two-month compositing time. Moreover, if missing data persists for a few pixels during the critical time window, it will not significantly impact landslide detection. In cases where the NDVI time series contains gaps due to cloud cover, the algorithm simply skips the affected time step and proceeds to the next available observation. The landslide is then identified based on the difference between this new time step and the previous valid observation.

The cloud-free composite images were successively employed to compute Normalized Difference Vegetation Index (NDVI) [29] time series datasets, which are instrumental in landslide detection. NDVI is computed using the band ratio of the near-infra-red (NIR) and red bands of optical imagery. To further improve the detection algorithm and diminish the influence of noise within the NDVI time series, we implemented a moving-window smoothing technique (Equation (1)) to the NDVI time series. The width of the moving window is set for three time steps or three images, with either individual images or monthly or bimonthly varying for each distinct case. Given that temporal resolution and vegetation recovery rates differ across study areas, a three-time-step smoothing approach was chosen to ensure a balanced trade-off between data continuity and data smoothing for precise RIL detection.

$$\text{NDVI}_t(x, y) = \frac{1}{k+1} \sum_{j=-\frac{k}{2}}^{\frac{k}{2}} \text{NDVI}_{t+j}(x, y) \quad (1)$$

where $\bar{NDVI}_t(x, y)$ is the smoothed value within the moving window for pixel (x, y) at time t . $t = \frac{k}{2} + 1, \frac{k}{2} + 2, \dots, l - k/2$, $NDVI_t(x, y)$ is the NDVI value for pixel (x, y) at time t . k is the width of the moving window and l is the size of the NDVI time series.

B. GPM-IMERG rainfall data

The Integrated Multi-satellite Retrievals for Global Precipitation Measurement GPM (IMERG) data were obtained from GEE, offering high temporal resolution (3-hourly) and moderate spatial resolution (~ 11 km). The study focused on 7-day antecedent rainfall (AR) to establish a direct link between intense precipitation events and observed landslides. The cumulative AR was calculated in GEE and subsequently used to filter significant rainfall events contributing to RIL occurrences. Historical rainfall data were used to identify extreme precipitation events likely to trigger landslides.

2.2.2. Landslide Detection Using Satellite Time Series Data

Landslides, particularly in vegetated landscapes, are distinctively established as abrupt declines in NDVI values due to the exposure of bare soil and bedrock. This results in a pronounced scar that endures until the vegetation recovers [24,30]. By analyzing the temporal gradient of the NDVI time series, we can efficiently detect landscapes where vegetation cover has experienced sudden and significant decline, indicative of landslide events (Equation (2)); thus, a minimum threshold (m) of 0.3 is set for all the cases. We posit that landslides, rather than seasonal vegetation patterns such as the deciduous leaf-off effect, are primarily responsible for the observed decline in NDVI since the study locations are mostly confined to subtropical zones [31]. We mapped out water bodies such as reservoirs and rivers since the fluctuating water levels along the banks can also cause abrupt changes in NDVI.

$$-\frac{d}{dt}\bar{NDVI}_t(x, y) > m \quad (2)$$

$$AR_t(x, y) > n \quad (3)$$

Here, m is the minimum tolerance for the NDVI temporal gradient. n is the minimum tolerance for the 7-day antecedent rainfall. $AR_t(x, y)$ is the 7-day antecedent rainfall value for pixel (x, y) at time t .

$$AR_t(x, y) = \sum_{i=0}^6 R_{t-i}(x, y) \quad (4)$$

where R_t is the cumulative rainfall for each day for 7-day antecedent rainfall.

Analogous to the NDVI analysis, we integrated GPM-IMERG (Integrated Multi-satellite Retrievals for Global Precipitation Measurements) data to identify landslides specifically triggered by rainfall. Every three hours, GPM provides significant data on global rainfall and snowfall, using the IMERG unified algorithm merging the data from all passive-microwave instruments at about 11 km spatial resolution. IMERG outperforms other satellite products in terms of producing spatio-temporal patterns and variations in intense precipitation, particularly at larger time steps (weeks, months, and years) [32–34]. Firstly, a dataset of 7-day antecedent rainfall (AR) was computed in GEE (Equation (4)), aggregated at weekly intervals, to acquire all significant rainfall events across the study period since the majority of landslide events are triggered within hours to a few days from the start of intense rainfall [35,36]. Furthermore, the rainfall events that exceeded the 90th percentile, set as n in Equation (3), were classed as intense [37] and were subsequently correlated with the prospective landslide events identified in the NDVI time series (Figure 3). Each time a landslide event was identified in the NDVI time series at a time ' t ', we conducted a temporal search for the conforming intense rainfall events within the time interval ' t ' and ' $t - \Delta t$ ', where Δt is the time frame (monthly or bimonthly) used to generate

the Sentinel-2 composites for each particular case study. This approach facilitated a robust temporal linkage between intense rainfall events and consequent landslide occurrences.

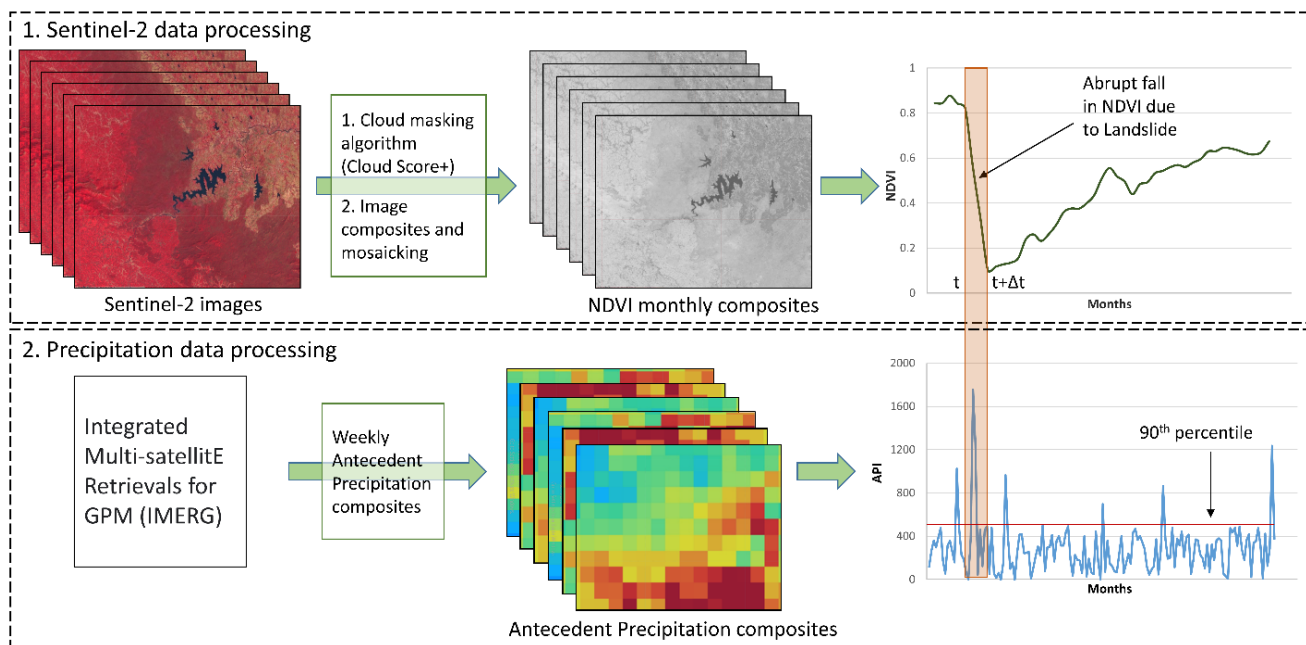


Figure 3. Schematic outline of the processing steps for Sentinel-2 and IMERG rainfall datasets.

2.2.3. Spatial Accuracy and Uncertainty

To evaluate the effectiveness of integrating optical imagery with rainfall data for detecting rainfall-induced landslides (RILs), we conducted a rigorous validation of the algorithm's output against multiple landslide inventories. The validation methodology varied depending on the inventory format, whether polygon-based or point-based. For polygon inventories, we employed spatial intersection and overlay analyses, quantifying the agreement between algorithm-detected landslides and mapped inventories. From these, we derived the following performance metrics commonly used in remote sensing and classification validation. User's Accuracy (UA): The reliability of detected landslides, defined as $TP/(TP + FP)$, representing the proportion of correctly classified landslide pixels relative to all predicted landslides. Producer's Accuracy (PA): The completeness of landslide detection, calculated as $TP/(TP + FN)$, measuring the proportion of actual landslides correctly identified by the algorithm. F1-Score: A balanced metric accounting for both UA (precision) and PA (recall), computed as $2 \times (UA \times PA)/(UA + PA)$, which provides a harmonic mean of the two accuracies, ensuring a comprehensive evaluation of detection performance.

For point-based inventories, where landslides were recorded as discrete points rather than polygons, we assessed accuracy by determining the proportion of inventory points that fell within algorithm-detected landslide polygons. In this case, TP, FP, and FN values are expressed as percentages, indicating the proportion of matched or misclassified points relative to the total. Table 3 presents a comparative analysis of the proposed algorithm against existing inventories. For polygon inventories, TP, FP, and FN are reported in square meters (m^2), representing detected, misclassified, and missed landslide areas, respectively. For point-based inventories, these metrics are expressed as percentages to reflect the proportion of correctly identified landslides. This approach ensures a robust and spatially explicit assessment of model performance across diverse geographic regions and data sources, highlighting the algorithm's ability to generalize across varying landscape conditions.

Table 3. Comparison of proposed algorithm and previously mapped inventories based on overlapping landslide area.

Location	Inventory Type	UA	PA	F1-Score
Hiroshima		0.80	0.85	0.82
Itogon		0.80	0.89	0.83
Mature	Polygon	0.76	0.85	0.80
Yilan		0.87	0.92	0.89
Thrissur		0.82	0.88	0.85
Phonxay		0.80	0.88	0.83
Paung	Point	0.77	0.85	0.79
Huong Viet		0.84	0.92	0.86

3. Results

3.1. RIL Detection Using NDVI Time Series

The integration of the NDVI time series analysis with rainfall data has yielded insights into RIL detection across diverse geographical settings. Figure 4 illustrates the variability of vegetation profile in different cases, showcasing three different scenarios of NDVI time series in the detection of RILs. Figure 4 demonstrates the visual difference in FCC images for three distinct landslide cases, namely (a) Kodagu (India), (b) Hiroshima (Japan), and (c) Mutare (Zimbabwe) spanning distinct climate and geographical settings. The Kodagu and Hiroshima RILs depict the typical pattern of a landslide-affected vegetation profile before and after the occurrence (Figure 4d). The steep decline in the NDVI value, if analogous to the intense rainfall event, can be identified as RIL. The vegetation recovery following the landslide occurrence, however, may demonstrate a disparity, as the Kodagu landslide does not show any significant regrowth several years after the occurrence, whereas quick regrowth is observed in the Hiroshima landslide.

Contrary to the relatively uncomplicated cases mentioned above, the vegetation pattern observed in the case of Mutare RILs in Zimbabwe is quite different (Figure 4d). Being in the humid subtropical climate, seasonal fluctuations in vegetation patterns are observed due to pronounced wet and dry seasons (NDVI time series ‘c’ in Figure 4d). The sub-section of the Mutare RIL NDVI time series (within the black box in Figure 4e) focuses on this complexity, demonstrating the use of the integration of the AR (antecedent rainfall) in the precise marking of RIL from the vegetation patterns. For instance, prospective event 1 (marked as a black triangle in Figure 4d) is ruled out as a landslide due to the absence of a corresponding extreme rainfall event within the defined time window, while prospective event 2 is confirmed as RIL because of the co-occurrence of a sharp NDVI decline with significant rainfalls (marked with red bars). Using only NDVI time series to detect landslides may lead to errors, as vegetation changes can be influenced by various factors. However, incorporating rainfall data improves accuracy by providing a crucial triggering factor. Heavy rainfall is often a primary cause of landslides, leading to sudden vegetation loss detected in NDVI. By analyzing both data, it becomes easier to distinguish actual landslides from seasonal vegetation changes or agricultural activities. This integrated approach enhances landslide detection reliability.

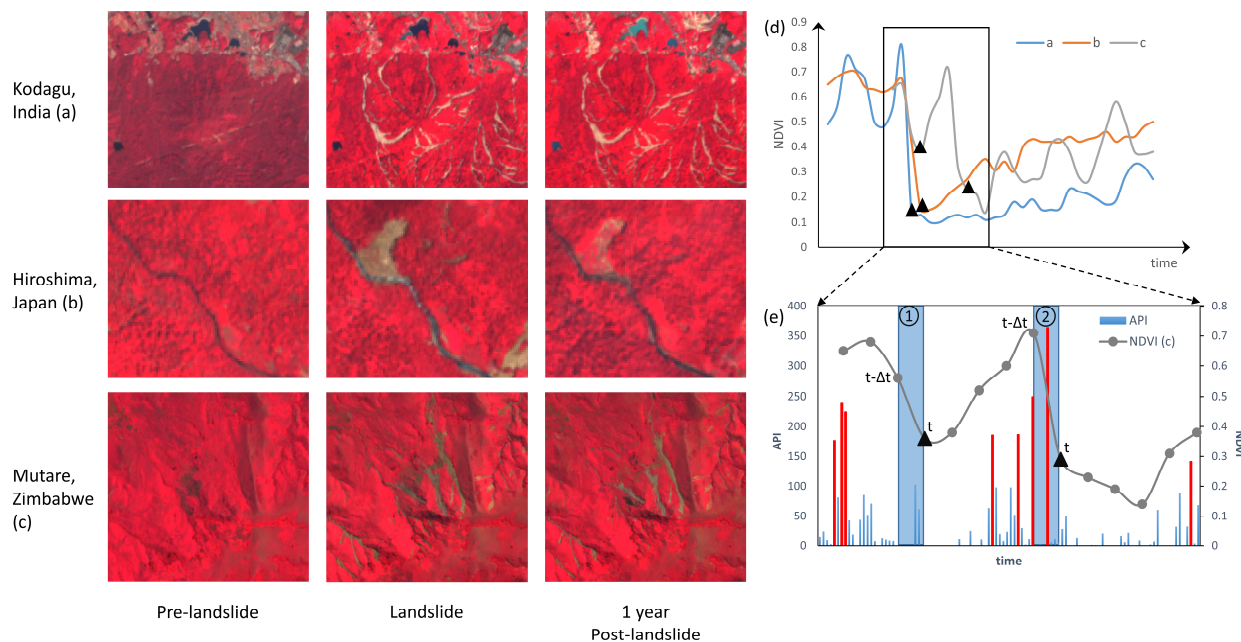


Figure 4. (a–c) shows the Sentinel-2 FCC images for pre-event, soon after a landslide, and 1-year after a landslide for three distinct cases. (d) displays the distinct NDVI profile of one of the landslides from each case, and (e) is a section of the NDVI time series for Mutare, Zimbabwe, typical of seasonal variations, explaining the detection of RIL from the prospective landslides (marked as black triangles). Prospective event 2 is confirmed as RIL, whereas prospective event 1 is not RIL.

3.2. Spatial Agreement of RIL Detection

The algorithm successfully detected a significant portion of landslides previously documented in the reference inventories, demonstrating the spatio-temporal accuracy of the algorithm. Despite the differences in the spatial as well as spectral fingerprints of the satellite images used in this study and those used for generating the inventories, the algorithm is capable of recognizing the RILs (Figure 4). The case-wise comparison and evaluation metrics of RIL detection are presented in Table 3. Accuracy metrics such as user accuracy (UA) and producer accuracy (PA) confirm that the algorithm was successful in detecting above 85% of the landslides, despite these metrics being based on the overlay (area-based) analysis. If the evaluation metrics are based on the intersection of some or any part of the inventory and the algorithm-detected RIL, a producer accuracy (PA) of greater than 95% was attained. The TP and PA are lower in cases with point inventory, which can be attributed to the inherent difference in the nature of polygon and point-based inventories. The algorithm performs reliably in detecting RILs, despite these spatial limitations.

Figure 5 showcases a few selected samples, one from each case, to illustrate the prediction of RILs with respect to the reference inventories. The discrepancies between the inventory and the detected RILs primarily stem from small landslides going undetected, as can be observed in Thissur (Figure 4a) and the Hiroshima case (Figure 4c), due to the reliance on openly available data. Apart from such inaccuracies, the algorithm's limitation to precisely identify the landslides that have been reactivated before vegetation regrowth resulted in some RILs left undetected, as the detection of RILs in this study is predominantly driven by identifying change points in the NDVI time series.

Despite some inaccuracies, there are instances where the algorithm outperformed the manual inventories and detected some landslides and mudflows that were previously overlooked. Figure 6 demonstrates an example of a large RIL with an approximate area of 10,000 sq. meters triggered on a steep slope during the September 2018 Typhoon Manghut rainfall. This RIL, located at the periphery of an open-cast mine, went undetected by the

manual inventory. The NDVI time series for a reference point within the RIL confirmed its association with the 2018 Typhoon Manghut and the Google Earth images before and after the event helped to establish it as a RIL.

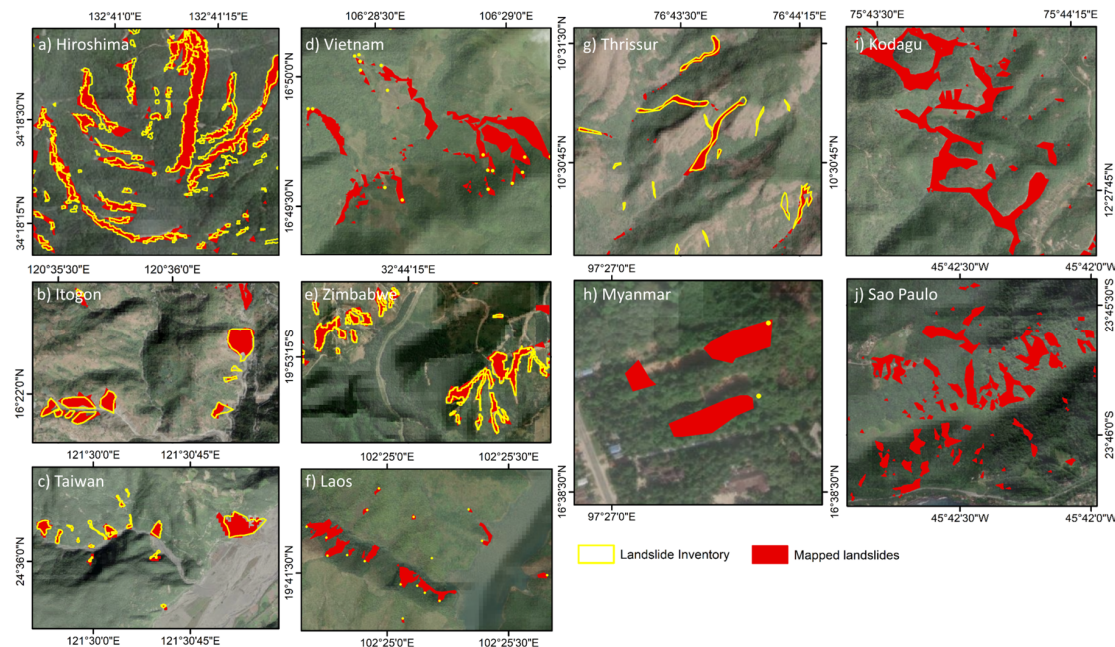


Figure 5. (a–j) are the RIL detections made by the proposed algorithm for all of the 10 cases, shown by red-color polygons. Polygons with yellow boundaries or yellow points are the mapped landslides from reference inventories. (i,j) are mapped RILs in this study and do not have reference inventories.

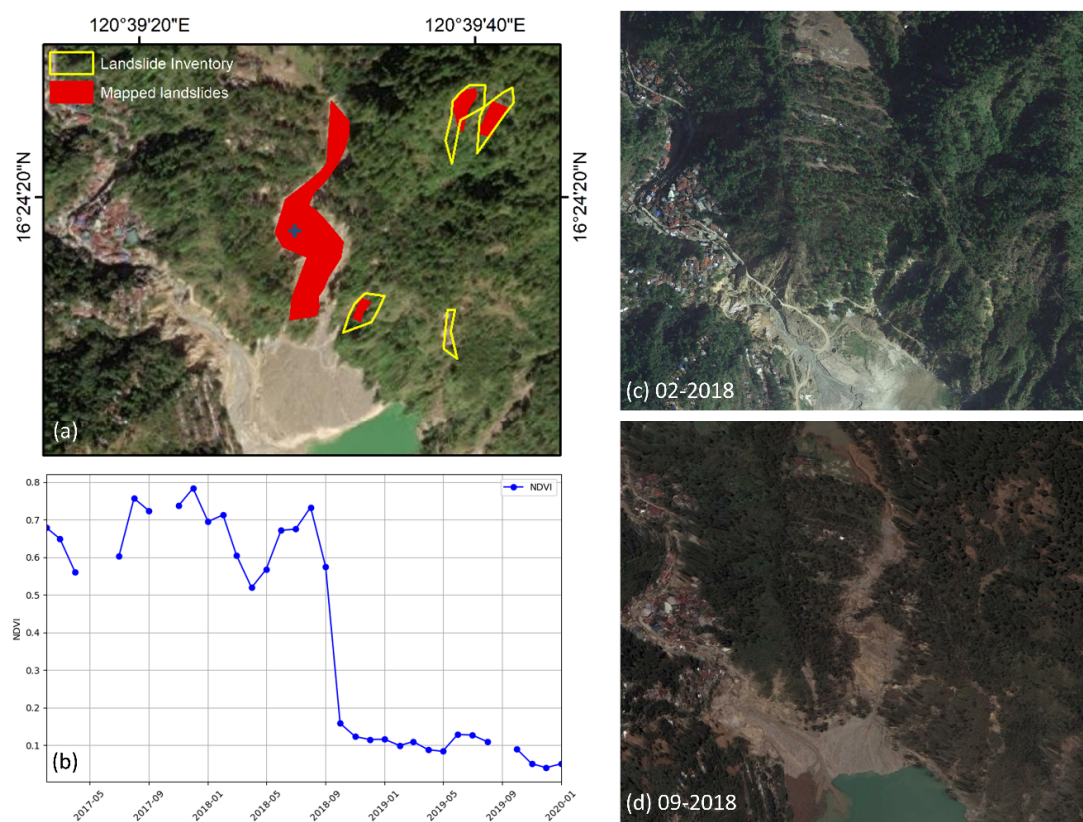


Figure 6. (a) An example of a large RIL detected by the algorithm that was left undetected by manually mapped inventory. (b) The time series of a sample pixel marked with a blue cross in (a). (c,d) are the Google Earth images of the same region captured before and after the RIL, respectively.

3.3. Frequency–Area Distribution

To better comprehend and compare the size and frequency of RILs across different landslide events, we plotted the frequency–area distribution plot for seven studied cases. Figure 6 illustrates that intense rainfall in Kodagu and Hiroshima triggered a greater number of large landslides than other cases, while Yilan and Thrissur have the fewest large landslides and lower frequency density. Table 2 presents the mean and maximum slope recorded for each case and the total event rainfall and hourly maximum rainfall during the event. The slope statistics are derived from the Copernicus 30 m Global Digital Elevation Model and the rainfall statistics are derived from the GPM-IMERG data. The pixel with the maximum precipitation in the Region of Interest is chosen for the hourly maximum rainfall for each case. During the Hiroshima event, hourly rainfall intensity at a particular ground station peaked at up to 70 mm/h [38], whereas, in Kodagu, the August 2018 rainfall was five times higher than the typical monthly average [39]. This extraordinary level of rainfall contributed to the scale and devastation of the landslides in these regions. The landslides in Kodagu and São Paulo, Brazil, were mapped in this study using 10 m resolution Sentinel-2 images. This moderate resolution is suitable for detecting medium to large landslides but tends to overlook smaller ones, which could explain the lower detection rates for small-scale RILs in these regions. Specifically, in Thrissur, a relatively small number of RILs were recorded and the size-density plot clearly highlights this lower density of landslides. Likewise, in Yilan, the rainfall produced only a few yet notably large landslides in the region.

The power-law distribution of these RILs varies significantly below the threshold of 10,000 m², which can be attributed to the differences in mapping resolution (Figure 7). Notably, apart from Hiroshima, none of the inventories exhibit a clear power-law scaling, likely because the inventories are not complete, and it recorded the landslides occurred from a particular event, confined to a city/district or the extent of high-resolution images available rather than documenting all the triggered landslides. The challenge of accurately mapping RILs is exacerbated by the persistent cloud cover in the affected regions, making it difficult to capture the full extent of the landslides. Nonetheless, all these events being triggered by extreme rainfall, the variation in landslide size, and the distribution across different locations points to the influence of other underlying factors, such as slope gradient, aspect, lithology, vegetation, etc., in addition to rainfall [8,16,20,40].

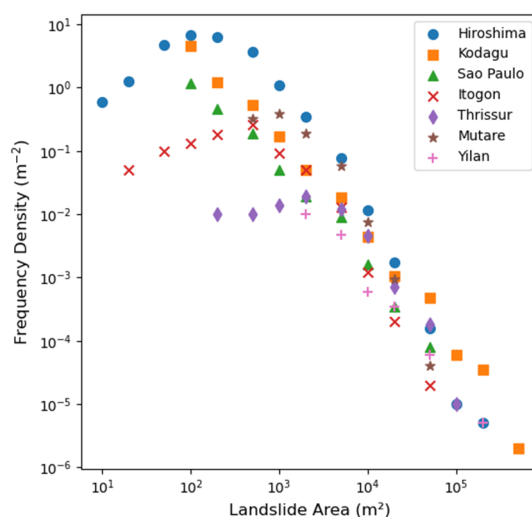


Figure 7. Plots of the frequency density distribution of landslide size for the various analyzed cases. The power-law fits in the cases are shown in Appendix A.

4. Discussion

4.1. Integration of Sentinel-2 and IMERG Time Series Data

The derivation of quick and accurate landslide inventories is a key research challenge in landslide studies, particularly for RILs, which are further challenging to map due to the dominance of clouds during extreme rainfall, typhoons, and tropical storms. This study proposed a combination of the Sentinel-2 freely available moderate-resolution data time series and the rainfall time series from GPM_IMERG to precisely map the RILs. The semi-automated time series data algorithm used for the analysis offers an advantage over traditional bi-temporal data in choosing the appropriate images, reducing potential bias in this ever-changing landscape. Using pre- and post-event images requires precision in selecting appropriate imagery, and in many cases, a single-time image may not capture all landslides due to cloud cover. The proposed algorithm addresses this limitation by utilizing image composites and a series of images for landslide detection. If a landslide pixel is masked due to cloud cover, the algorithm leverages adjacent images to reconstruct the NDVI profile, ensuring more complete detection. Optical remote sensing satellites are instrumental in the precise monitoring of land surface changes and dynamics, providing crucial data to study geomorphic and natural hazards [23,41]. The Landsat mission and Sentinel-2 are the two most commonly employed satellites for such studies as they provide open access data and a favorable spatio-temporal resolution for analyzing land surface dynamics [30,42–46]. While Sentinel-2 lacks the extensive historical data offered by Landsat, it is ideal for studying events since 2015 due to its higher spatial resolution of 10 m and a much shorter revisit time of 5 days.

Previous studies have highlighted the potential of NDVI for detecting landslides since it captures vegetation health and density, rendering it sensitive to abrupt changes in land surface, such as those caused by landslides [23,47,48]. However, the NDVI values are often adversely affected by either clouds and weather conditions or abrupt anthropogenic changes in land cover. The cloud masking and moving window smoothing techniques can diminish the impact of the former; however, the abrupt changes in the NDVI time series can be caused due to some anthropogenic activity and appear to be landslide-induced changes. Taking advantage of both Sentinel-2 and GPM-IMERG rainfall data, we have proposed a framework to identify the RILs using the integration of NDVI variations and extreme rainfall events. Therefore, any abrupt decline in NDVI due to anthropogenic activity, outside the rainfall event, will not be detected as RIL. Secondly, such activities are most common on flat land or gentle slopes, whereas landslides are typical to steep slopes [7,43,49]; therefore, of all the landslides detected by the integration of Sentinel-2 and IMERG, only those that occurred on slopes steeper than 10° are considered as RILs. While the factors determining the power-law distribution of landslides remain uncertain, there is growing evidence that topography, along with the rocks' mechanical properties, must be one of the key controlling elements [50]. Future rainfall patterns, driven by climate change, are expected to significantly increase the RIL risk. Escalating global temperatures are expected to strengthen and increase the frequency of extreme rainfall events, which might lead to larger and more frequent landslides. Consequently, studies predicted that under the SSP2-4.5 scenario, the global average annual casualty risk is projected to grow by 140% during the 2031–2060 period and 160% by 2066–2095 [51].

4.2. Uncertainties in Detected RILs

Overall, the proposed algorithm is simple and efficient and uses open-access data with near-global coverage to detect RILs with comparable quality to costly and time-consuming inventories. Seasonal variations in vegetation, climatic conditions, and vegetation type have a significant impact on vegetation growth and coverage. These variations differ globally,

making it challenging to have an established and universal threshold for post-landslide NDVI decline [48]. This absence of a standardized threshold leads to landslides left undetected as the pre- and post-landslide NDVI does not follow any particular pattern [52,53]. This challenge is further compounded by the rapid vegetation recovery in some shallow landslides and debris flow when coalesced to the lack of timely data after landslides or gaps due to cloud cover or the long revisit frequency of satellites. Therefore, all such circumstances can hinder the detection of RILs, and the accuracy of landslide detection using NDVI changes is compromised.

A few studies also utilized harmonic and sinusoidal modeling to monitor such NDVI changes; however, it requires extensive calibration and varies significantly across climatic zones [30,54]. The proposed algorithm presents a simple and effective approach for detecting the RILs based on their occurrence that is synchronous to intense rainfall events. In most cases, the F1-score of RIL detection is above 0.8, demonstrating the efficiency of this approach. Most of the studied landslide cases are located in subtropical climates and, therefore, produce good results; however, Mutare is located in a subtropical savanna climate zone and typically has seasonal vegetation fluctuations; hence, the accuracy is lower than other cases. Another case in Paung, Myanmar, also resulted in lower accuracy, most likely due to the point-based nature of the inventory used for validation, as the inventory was derived using the landslide initiation points from the highest elevation on the landslide boundary using the high-resolution images [27]. Furthermore, the high-resolution satellite images utilized to generate such inventories may result in a mismatch with the 10 m resolution of Sentinel-2 images.

The detection of landslides in steep, high-elevation regions, particularly in temperate zones, poses challenges due to the terrain shadow effects. These shadows reduce the surface reflectance of vegetated terrain in a few images, resulting in low NDVI values, which could be falsely interpreted by algorithms as abrupt declines in NDVI, thus resulting in false landslide detections. Such limitations highlight the importance of precise image selection techniques, where manually choosing pre- and post-event images often outperforms automated time series analysis, particularly in these challenging terrains [17,55]. However, in tropical and subtropical zones, where terrain shadows are less prominent, algorithms perform better with time series data [23,24,56]. Additionally, human influences on landcover dynamics, particularly on flat land and gentle slopes, further complicate landslide detection. Human activities such as deforestation or land-use changes may generate abrupt changes in NDVI, imitating the spectral signature of landslides. To mitigate these challenges, this research focuses on slopes of 10° and above, where human intervention is less likely to distort vegetation dynamics [49,57]. These considerations help improve the accuracy and reliability of RIL detection in the study regions. Nonetheless, there are avenues of improvement by further enhancing the pixel-wise analysis using machine learning techniques.

5. Conclusions

Earth observation provides large-scale, near-real-time monitoring, enabling decision-makers to analyze human–environment interactions, assess risks, and develop effective mitigation strategies. By integrating global geospatial data, we can improve our understanding of where and when landslides are likely to occur, enhancing disaster preparedness. This study proposed a systematic change detection algorithm for detecting and mapping rainfall-induced landslides (RILs) using Sentinel-2 imagery and combined with rainfall time series from GPM IMERG. The semi-automated time series algorithm offers a key advantage over traditional bi-temporal methods by selecting appropriate images, minimizing potential bias, and addressing the challenges posed by dynamic landscapes. The algorithm

was evaluated using both manually mapped landslide inventories and high-resolution data-based inventories, demonstrating the effectiveness of the Sentinel-2 time series for RIL analysis. The achieved overall F1-score of 0.82, along with producer accuracies exceeding 84% across all inventories, highlights its reliability. The highest inaccuracies were observed in the Mutare region, likely due to its pronounced seasonal variations and the distinct wet–dry cycles that are characteristic of a subtropical savanna climate. The high false-positive values are attributed to the use of high-resolution data (3 m or 5 m) for validation inventories. In contrast, the coarser pixel resolution of Sentinel-2 results in the overestimation of landslide extent. Notably, the algorithm successfully detected several RILs that remained unreported in manual inventories, with strong validation through vegetation profiles and morphometric characteristics.

Beyond detecting individual events, this method can further enable the estimation of landslide frequency in RIL-prone regions by leveraging the long-term Sentinel-2 archive (2015–present). By analyzing historical landslide occurrences, it is possible to identify the spatial and temporal patterns of RIL events, offering valuable insights into their recurrence and helping in identifying the controlling factors that drive landslide activity for mitigation strategies. Overall, the proposed algorithm is simple, efficient, and utilizes open-access data with near-global coverage, providing a cost-effective alternative to traditional, labor-intensive landslide inventories. Future improvements can be explored by incorporating machine learning techniques to enhance pixel-wise analysis and further refine RIL detection accuracy.

Author Contributions: Conceptualization, H.-J.C. and M.A.A.; methodology, M.A.A.; validation, M.A.A., S.R.P. and V.K.; writing—original draft preparation, M.A.A.; writing—review and editing, H.-J.C.; supervision, H.-J.C. All authors have read and agreed to the published version of the manuscript.

Funding: This research was funded by NSTC, Taiwan, grant number 113-2621-M-006-002- and 113-2121-M-006-011-.

Data Availability Statement: The datasets used for analysis can be accessed from the Google Earth Engine (GEE) code editor <https://code.earthengine.google.com/>. The datasets generated in this study are available from the corresponding author on request. The GEE python code algorithm defined in this study is available from the corresponding author on request.

Conflicts of Interest: The authors declare no conflicts of interest.

Appendix A

Fitting a landslide-event inventory to a power-law distribution:

The power-law distribution suggests that smaller landslides occur more often, whereas larger ones are less frequent but have a significant impact when they do occur. The power-law distribution can describe the relationship between the frequency of landslides and their magnitudes [58],

$$p(X) = c10^{mLS} X^{-\beta} \quad (\text{A1})$$

where c is a constant obtained by dividing the normalization constant by the total number of landslides, mLS is landslide-event magnitude scale, β is the power-law exponent, X is landslide area, and $p(X)$ is the frequency density of landslides.

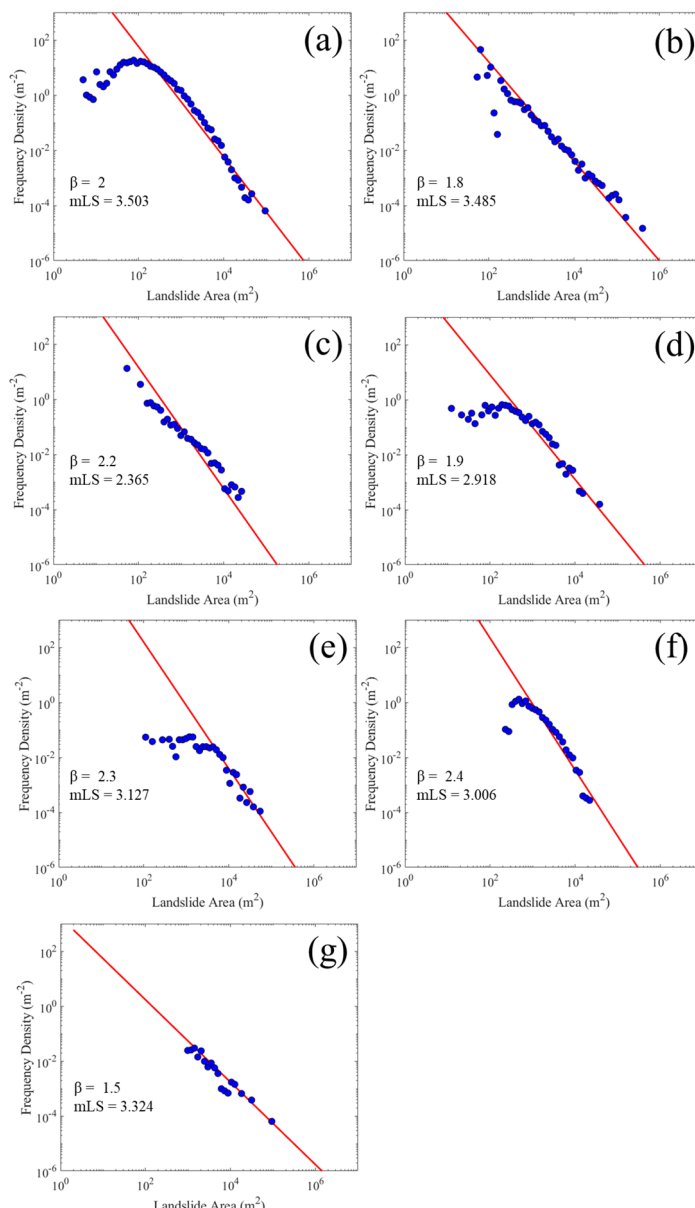


Figure A1. Fitting of a landslide-event inventory to a power-law distribution in (a). Hiroshima, (b). Kodagu, (c). Sao Paulo, (d). Itogon, (e). Thrissur, (f). Mutare, and (g). Yilan.

References

1. Varnes, D.J. Landslides Types and Processes. In *Landslides and Engineering Practices*; Highway Research Board: Washington, DC, USA, 1958; p. 232, ISBN 0-598-74265-4.
2. Larsen, I.J.; Montgomery, D.R.; Korup, O. Landslide Erosion Controlled by Hillslope Material. *Nat. Geosci.* **2010**, *3*, 247–251. [[CrossRef](#)]
3. Clague, J.J.; Stead, D. *Landslides: Types, Mechanisms and Modeling*; Cambridge University Press: Cambridge, UK, 2012; ISBN 978-1-107-00206-7.
4. Crozier, M.J. Multiple-Occurrence Regional Landslide Events in New Zealand: Hazard Management Issues. *Landslides* **2005**, *2*, 247–256. [[CrossRef](#)]
5. Aristizábal, E.; Korup, O. Linking Landslide Patterns to Transient Landscapes in the Northern Colombian Andes. *J. Geophys. Res. Earth Surf.* **2025**, *130*, e2024JF008027. [[CrossRef](#)]
6. Cardona, F.G.; Giraldo, E.A.; Arango, M.I.; Mergili, M. Regional and Detailed Multi-Hazard Assessment of Debris-Flow Processes in the Colombian Andes. In Proceedings of the EGU General Assembly 2021, Online, 19–30 April 2021.
7. Yang, S.-Y.; Jan, C.-D.; Wang, J.-S.; Yang, S.-Y.; Jan, C.-D.; Wang, J.-S. Landslides Triggered by Typhoon Morakot in Taiwan. In *Environmental Risks*; IntechOpen: London, UK, 2018; ISBN 978-1-78984-224-1.
8. Cullen, C.A.; Al Suhili, R.; Aristizabal, E. A Landslide Numerical Factor Derived from CHIRPS for Shallow Rainfall Triggered Landslides in Colombia. *Remote Sens.* **2022**, *14*, 2239. [[CrossRef](#)]

9. Froude, M.J.; Petley, D.N. Global Fatal Landslide Occurrence from 2004 to 2016. *Nat. Hazards Earth Syst. Sci.* **2018**, *18*, 2161–2181. [[CrossRef](#)]
10. Casagli, N.; Intrieri, E.; Tofani, V.; Gigli, G.; Raspini, F. Landslide Detection, Monitoring and Prediction with Remote-Sensing Techniques. *Nat. Rev. Earth Environ.* **2023**, *4*, 51–64. [[CrossRef](#)]
11. CRED. *Economic Losses, Poverty & Disasters 1998–2017*; Université Catholique de Louvain (UCL): Ottignies-Louvain-la-Neuve, Belgium, 2018.
12. Gómez, D.; García, E.F.; Aristizábal, E. Spatial and Temporal Landslide Distributions Using Global and Open Landslide Databases. *Nat. Hazards* **2023**, *117*, 25–55. [[CrossRef](#)]
13. Angeli, M.-G.; Pasuto, A.; Silvano, S. A Critical Review of Landslide Monitoring Experiences. *Eng. Geol.* **2000**, *55*, 133–147. [[CrossRef](#)]
14. Guzzetti, F.; Mondini, A.C.; Cardinali, M.; Fiorucci, F.; Santangelo, M.; Chang, K.-T. Landslide Inventory Maps: New Tools for an Old Problem. *Earth-Sci. Rev.* **2012**, *112*, 42–66. [[CrossRef](#)]
15. Merghadi, A.; Yunus, A.P.; Dou, J.; Whiteley, J.; ThaiPham, B.; Bui, D.T.; Avtar, R.; Abderrahmane, B. Machine Learning Methods for Landslide Susceptibility Studies: A Comparative Overview of Algorithm Performance. *Earth-Sci. Rev.* **2020**, *207*, 103225. [[CrossRef](#)]
16. Emberson, R.; Kirschbaum, D.B.; Amatya, P.; Tanyas, H.; Marc, O. Insights from the Topographic Characteristics of a Large Global Catalog of Rainfall-Induced Landslide Event Inventories. *Nat. Hazards Earth Syst. Sci.* **2022**, *22*, 1129–1149. [[CrossRef](#)]
17. Milledge, D.G.; Bellugi, D.G.; Watt, J.; Densmore, A.L. Automated Determination of Landslide Locations after Large Trigger Events: Advantages and Disadvantages Compared to Manual Mapping. *Nat. Hazards Earth Syst. Sci.* **2022**, *22*, 481–508. [[CrossRef](#)]
18. Meunier, P.; Hovius, N.; Haines, J.A. Topographic Site Effects and the Location of Earthquake Induced Landslides. *Earth Planet. Sci. Lett.* **2008**, *275*, 221–232. [[CrossRef](#)]
19. Rault, C.; Robert, A.; Marc, O.; Hovius, N.; Meunier, P. Seismic and Geologic Controls on Spatial Clustering of Landslides in Three Large Earthquakes. *Earth Surf. Dyn.* **2019**, *7*, 829–839. [[CrossRef](#)]
20. Aristizábal, E.; Vélez, J.I.; Martínez, H.E.; Jaboyedoff, M. SHIA_Landslide: A Distributed Conceptual and Physically Based Model to Forecast the Temporal and Spatial Occurrence of Shallow Landslides Triggered by Rainfall in Tropical and Mountainous Basins. *Landslides* **2016**, *13*, 497–517. [[CrossRef](#)]
21. Kirschbaum, D.; Stanley, T.; Zhou, Y. Spatial and Temporal Analysis of a Global Landslide Catalog. *Geomorphology* **2015**, *249*, 4–15. [[CrossRef](#)]
22. Delforge, D.; Watheler, V.; Below, R.; Sofia, C.L.; Tonnelier, M.; Loenhout, J.A.F.; Speybroeck, N. EM-DAT: The Emergency Events Database. 2025. Available online: <https://www.researchsquare.com/article/rs-3807553/v2> (accessed on 3 March 2025).
23. Behling, R.; Roessner, S.; Golovko, D.; Kleinschmit, B. Derivation of Long-Term Spatiotemporal Landslide Activity—A Multi-Sensor Time Series Approach. *Remote Sens. Environ.* **2016**, *186*, 88–104. [[CrossRef](#)]
24. Aman, M.A.; Chu, H.-J.; Yunus, A.P. Exploration of Multi-Decadal Landslide Frequency and Vegetation Recovery Conditions Using Remote-Sensing Big Data. *Earth Syst. Environ.* **2024**, *9*, 197–213. [[CrossRef](#)]
25. Zhu, Z.; Wulder, M.A.; Roy, D.P.; Woodcock, C.E.; Hansen, M.C.; Radeloff, V.C.; Healey, S.P.; Schaaf, C.; Hostert, P.; Strobl, P.; et al. Benefits of the Free and Open Landsat Data Policy. *Remote Sens. Environ.* **2019**, *224*, 382–385. [[CrossRef](#)]
26. Notti, D.; Cignetti, M.; Godone, D.; Giordan, D. Semi-Automatic Mapping of Shallow Landslides Using Free Sentinel-2 Images and Google Earth Engine. *Nat. Hazards Earth Syst. Sci.* **2023**, *23*, 2625–2648. [[CrossRef](#)]
27. Amatya, P.; Kirschbaum, D.; Stanley, T. Rainfall-Induced Landslide Inventories for Lower Mekong Based on Planet Imagery and a Semi-Automatic Mapping Method. *Geosci. Data J.* **2022**, *9*, 315–327. [[CrossRef](#)]
28. Google Earth. All Clear with Cloud Score+. *Google Earth Engine*. 2024. Available online: <https://medium.com/google-earth/all-clear-with-cloud-score-bd6ee2e2235e> (accessed on 3 March 2025).
29. Tucker, C.J. Red and Photographic Infrared Linear Combinations for Monitoring Vegetation. *Remote Sens. Environ.* **1979**, *8*, 127–150. [[CrossRef](#)]
30. Deijns, A.A.J.; Bevington, A.R.; van Zadelhoff, F.; de Jong, S.M.; Geertsema, M.; McDougall, S. Semi-Automated Detection of Landslide Timing Using Harmonic Modelling of Satellite Imagery, Buckinghorse River, Canada. *Int. J. Appl. Earth Obs. Geoinf.* **2020**, *84*, 101943. [[CrossRef](#)]
31. Wen, T.-H.; Teo, T.-A. Landslide Inventory Mapping from Landsat-8 NDVI Time Series Using Adaptive Landslide Interval Detection. *ISPRS Ann. Photogramm. Remote Sens. Spat. Inf. Sci.* **2022**, *3*, 557–562. [[CrossRef](#)]
32. Pradhan, R.K.; Markonis, Y.; Vargas Godoy, M.R.; Villalba-Pradas, A.; Andreadis, K.M.; Nikolopoulos, E.I.; Papalexiou, S.M.; Rahim, A.; Tapiador, F.J.; Hanel, M. Review of GPM IMERG Performance: A Global Perspective. *Remote Sens. Environ.* **2022**, *268*, 112754. [[CrossRef](#)]
33. Pan, X.; Wu, H.; Chen, S.; Nanding, N.; Huang, Z.; Chen, W.; Li, C.; Li, X. Evaluation and Applicability Analysis of GPM Satellite Precipitation over Mainland China. *Remote Sens.* **2023**, *15*, 2866. [[CrossRef](#)]

34. Tang, G.; Clark, M.P.; Papalexiou, S.M.; Ma, Z.; Hong, Y. Have Satellite Precipitation Products Improved over Last Two Decades? A Comprehensive Comparison of GPM IMERG with Nine Satellite and Reanalysis Datasets. *Remote Sens. Environ.* **2020**, *240*, 111697. [[CrossRef](#)]
35. Aleotti, P. A Warning System for Rainfall-Induced Shallow Failures. *Eng. Geol.* **2004**, *73*, 247–265. [[CrossRef](#)]
36. Kim, S.W.; Chun, K.W.; Kim, M.; Catani, F.; Choi, B.; Seo, J.I. Effect of Antecedent Rainfall Conditions and Their Variations on Shallow Landslide-Triggering Rainfall Thresholds in South Korea. *Landslides* **2021**, *18*, 569–582. [[CrossRef](#)]
37. Kirschbaum, D.; Stanley, T. Satellite-Based Assessment of Rainfall-Triggered Landslide Hazard for Situational Awareness. *Earth's Future* **2018**, *6*, 505–523. [[CrossRef](#)]
38. Hashimoto, R.; Tsuchida, T.; Moriwaki, T.; Kano, S. Hiroshima Prefecture Geo-Disasters Due to Western Japan Torrential Rainfall in July 2018. *Soils Found.* **2020**, *60*, 283–299. [[CrossRef](#)]
39. Kushal, M.; Barman, S.D. Kodagu Disaster (Floods-Emphasis on Catchment Fragmentation Index and Unscientific Land Usage) Analysis Using GIS. *IOP Conf. Ser. Earth Environ. Sci.* **2022**, *1032*, 012036. [[CrossRef](#)]
40. Yunus, A.P.; Sajinkumar, K.S.; Gopinath, G.; Subramanian, S.S.; Kaushal, S.; Thanveer, J.; Achu, A.L.; Islam, S.M.U.; Ishan, A.; Krishnapriya, V.K.; et al. Chronicle of Destruction: The Wayanad Landslide of July 30, 2024. *Landslides* **2025**. [[CrossRef](#)]
41. Nichol, J.; Wong, M.S. Satellite Remote Sensing for Detailed Landslide Inventories Using Change Detection and Image Fusion. *Int. J. Remote Sens.* **2005**, *26*, 1913–1926. [[CrossRef](#)]
42. Aman, M.A.; Salman, M.S.; Yunus, A.P. COVID-19 and Its Impact on Environment: Improved Pollution Levels during the Lockdown Period—A Case from Ahmedabad, India. *Remote Sens. Appl. Soc. Environ.* **2020**, *20*, 100382. [[CrossRef](#)]
43. Yunus, A.P.; Fan, X.; Tang, X.; Jie, D.; Xu, Q.; Huang, R. Decadal Vegetation Succession from MODIS Reveals the Spatio-Temporal Evolution of Post-Seismic Landsliding after the 2008 Wenchuan Earthquake. *Remote Sens. Environ.* **2020**, *236*, 111476. [[CrossRef](#)]
44. Chen, X.; Avtar, R.; Umarhadi, D.A.; Louw, A.S.; Shrivastava, S.; Yunus, A.P.; Khedher, K.M.; Takemi, T.; Shibata, H. Post-Typhoon Forest Damage Estimation Using Multiple Vegetation Indices and Machine Learning Models. *Weather Clim. Extrem.* **2022**, *38*, 100494. [[CrossRef](#)]
45. Chusnay, W.N.; Chu, H.-J.; Tatas; Jaelani, L.M. Machine-Learning-Estimation of High-Spatiotemporal-Resolution Chlorophyll-a Concentration Using Multi-Satellite Imagery. *Sustain. Environ. Res.* **2023**, *33*, 11. [[CrossRef](#)]
46. Aman, M.A.; Chu, H.-J. Long-Term River Extent Dynamics and Transition Detection Using Remote Sensing: Case Studies of Mekong and Ganga River. *Sci. Total Environ.* **2023**, *876*, 162774. [[CrossRef](#)]
47. Mondini, A.C.; Guzzetti, F.; Reichenbach, P.; Rossi, M.; Cardinali, M.; Ardizzone, F. Semi-Automatic Recognition and Mapping of Rainfall Induced Shallow Landslides Using Optical Satellite Images. *Remote Sens. Environ.* **2011**, *115*, 1743–1757. [[CrossRef](#)]
48. Fu, S.; de Jong, S.M.; Hou, X.; de Vries, J.; Deijns, A.; de Haas, T. A Landslide Dating Framework Using a Combination of Sentinel-1 SAR and -2 Optical Imagery. *Eng. Geol.* **2024**, *329*, 107388. [[CrossRef](#)]
49. Iverson, R.M.; Reid, M.E.; LaHusen, R.G. Debris-Flow Mobilization from Landslides1. *Annu. Rev. Earth Planet. Sci.* **1997**, *25*, 85–138. [[CrossRef](#)]
50. Zhang, J.; van Westen, C.J.; Tanyas, H.; Mavrouli, O.; Ge, Y.; Bajrachary, S.; Gurung, D.R.; Dhital, M.R.; Khanal, N.R. How Size and Trigger Matter: Analyzing Rainfall- and Earthquake-Triggered Landslide Inventories and Their Causal Relation in the Koshi River Basin, Central Himalaya. *Nat. Hazards Earth Syst. Sci.* **2019**, *19*, 1789–1805. [[CrossRef](#)]
51. Wang, X.; Wang, Y.; Lin, Q.; Yang, X. Assessing Global Landslide Casualty Risk Under Moderate Climate Change Based on Multiple GCM Projections. *Int. J. Disaster Risk Sci.* **2023**, *14*, 751–767. [[CrossRef](#)]
52. Behling, R.; Roessner, S.; Kaufmann, H.; Kleinschmit, B. Automated Spatiotemporal Landslide Mapping over Large Areas Using RapidEye Time Series Data. *Remote Sens.* **2014**, *6*, 8026–8055. [[CrossRef](#)]
53. Saito, H.; Uchiyama, S.; Teshirogi, K. Rapid Vegetation Recovery at Landslide Scars Detected by Multitemporal High-Resolution Satellite Imagery at Aso Volcano, Japan. *Geomorphology* **2022**, *398*, 107989. [[CrossRef](#)]
54. Aufaristama, M.; Werff, H.v.d.; Botha, A.E.J.; Meijde, M.v.d. Global Landslide Finder: Detecting the Time and Place of Landslides with Dense Earth Observation Time Series. *GeoHazards* **2024**, *5*, 780–798. [[CrossRef](#)]
55. Qu, F.; Qiu, H.; Sun, H.; Tang, M. Post-Failure Landslide Change Detection and Analysis Using Optical Satellite Sentinel-2 Images. *Landslides* **2021**, *18*, 447–455. [[CrossRef](#)]
56. Gariano, S.L.; Guzzetti, F. Landslides in a Changing Climate. *Earth-Sci. Rev.* **2016**, *162*, 227–252. [[CrossRef](#)]
57. Stumpf, A.; Kerle, N. Object-Oriented Mapping of Landslides Using Random Forests. *Remote Sens. Environ.* **2011**, *115*, 2564–2577. [[CrossRef](#)]
58. Tanyaş, H.; Allstadt, K.E.; van Westen, C.J. An updated method for estimating landslide-event magnitude. *Earth Surf. Process. Landf.* **2018**, *43*, 1836–1847. [[CrossRef](#)]